NJC

PAPER

View Article Online
View Journal | View Issue

Check for updates

Cite this: *New J. Chem.*, 2024, **48**, 17150

Synthesis of perforated single-crystalline Mn_2O_3 microcubes for thermocatalytic applications†

Santra Merin Saju and Anuj A. Vargeese *

Received 22nd August 2024,
Accepted 10th September 2024

DOI: 10.1039/d4nj03709j

rsc.li/njc

Transition metal oxides (TMOs) are increasingly viable choices for catalytic applications because of their tendency to exhibit variable oxidation states depending on the chemical environment and the possibility of enhancing surface activity through morphology control. The development of efficient and cost-effective methods for the synthesis of TMOs with meso-to nanoscale morphologies and improved characteristics remains a significant challenge. Herein, we report a template-free synthesis strategy for the preparation of perforated mesoporous manganese(III) oxide microcubes (PMOM) through a morphology-conserved transformation of the precursor method. The formation of PMOM with cubic structures and pore sizes in the range of 20 nm was confirmed using scanning electron microscopy (SEM) and transmission electron microscopy (TEM). The Mn_2O_3 samples exhibited a Swiss cheese-like porous structure with a particle size of 0.70 to 1.2 μm. Furthermore, the catalytic activity of the synthesized PMOM samples on the thermocatalytic decomposition of ammonium perchlorate (AP), an oxidizer used in solid propellants, was investigated. The transition between Mn^{3+} to Mn^{2+} oxidation states facilitates the transfer of electrons, allowing the metal surface to act as an electron acceptor during the oxidation of water molecules. Due to the oxidation–reduction cycle occurring on the surface, a considerable number of electrons are available for promoting surface reactions. Thus, the (211) surface of PMOM enhanced the thermal decomposition of AP, and a plausible mechanism for this catalytic activity was proposed.

Introduction

The relatively close energy levels of the $(n-1)$d and ns orbitals allow transition metals to exhibit a variety of oxidation states in compounds.[1,2] The oxidation number of transition metal compounds, such as transition metal oxides (TMOs), varies depending on the chemical environment.[3–6] These properties enable TMOs to catalyze a wide range of chemical reactions, making them indispensable for environmental and industrial catalytic applications.[7–10] TMO catalysts with controlled morphologies exhibit distinct physical and chemical properties and high surface activities.[11] The presence of porosity enhances the surface area, leading to further improvement in surface activity.

Manganese (Mn) is a transition metal that forms different stoichiometric oxides, such as MnO, Mn_2O_3, Mn_3O_4, and MnO_2, which have extensive industrial and environmental applications.[2,12,13] Many industrial applications, such as magnetic storage, catalysis, ion exchange, molecular adsorption, and electronics,[14–18] demand the development of evenly sized, and shape-controlled manganese oxide particles. Among the reported manganese oxides, Mn_2O_3 is one of the least explored manganese oxides for catalytic applications.[18] Reportedly, ordered mesoporous Mn_2O_3 and Mn_3O_4 with crystalline walls[19] and Mn_2O_3 prepared using low-concentration precursors exhibit large surface areas.[20] Spherical Mn_2O_3 with crystalline pore walls reportedly exhibits enhanced oxygen reduction reaction (ORR) activity.[21] Hierarchical mesoporous oval- and straw-sheaf-shaped Mn_2O_3 with a high surface area exhibited better cycling stability for lithium-ion batteries.[22]

In this study, a morphology-conserved transformation method of the precursor was used for the synthesis of perforated mesoporous manganese(III) oxide microcubes (PMOM) under varying reaction conditions. The decomposition of ammonium perchlorate (AP), a commonly used oxidizer in composite solid propellants[23] and AP-based propellants are enhanced by the use of metals/metal oxides/TMOs.[24–26] Furthermore, Mn_2O_3 nanofibers[27] exhibited good catalytic activity on the thermal decomposition of AP.[28,29] Hence, the catalytic activity of this PMOM on the thermal decomposition of AP, was investigated. PMOM is anticipated to be a promising burn rate modifier for AP-based composite solid propellants and could potentially find significant catalytic applications in areas such as environmental catalysis,[30] light-harvesting,[31] anode materials,[32] and the reduction of aromatic compounds.

Laboratory for Energetic and Energy Materials Research (LEEMR), Department of Chemistry, National Institute of Technology Calicut, Kozhikode 673601, India. E-mail: aav@nitc.ac.in

† Electronic supplementary information (ESI) available. See DOI: https://doi.org/10.1039/d4nj03709j

Experimental section

Synthesis of PMOM

A precipitation method[33] was fine-tuned to prepare the PMOM. In a typical synthesis, manganese nitrate tetrahydrate, 0.02 M or 0.1 M, was dissolved in 100 mL distilled water in a three necked round bottom flask and heated until the temperature of the reaction mixture became 90 °C. After attaining the reaction temperature, the pH of the solution was raised to the required value by controlled addition (20 mL h^{-1}) of $NaHCO_3$ using a syringe pump. The reaction continued for 3 h after the attainment of pH, then was cooled to room temperature and stirred overnight. The precipitate was collected by decanting the reaction mixture, washed several times with distilled water and recollected by centrifugation. The precipitate was dried overnight in a hot air oven at 70 °C, and then calcined at 600 °C for 12 h to obtain the PMOM samples. The details of the materials and characterization techniques are provided in the ESI.†

Catalytic activity evaluation

The AP–PMOM mixture with 2% (by weight) manganese(III) oxide was prepared by mechanical mixing. These samples were used for thermal analysis and catalytic activity evaluation. The thermal decomposition of AP and catalytic decomposition of AP–PMOM mixtures were performed in a nitrogen environment using a PerkinElmer STA6000 thermogravimetric (TG) analyzer. An open alumina sample pan with a volume of 100 μL was loaded with approximately 1–2 mg of the AP–PMOM mixture and non-isothermally heated at a heating rate of 8 °C min^{-1}. The obtained thermograms were analyzed to understand the catalytic effect of PMOM on the thermal decomposition of AP.

Results and discussion

Synthesis and characterization of perforated mesoporous manganese(III) oxide micro cubes (PMOM)

The effects of precursor concentration and reaction pH on the synthesis of Mn_2O_3 were systematically investigated, as listed in Table 1. The samples were prepared with a concentration of 0.1 M manganese nitrate precursor at pH 8 and 9 and identified as PMOM-P8 A and PMOM-P9 B, respectively. Another set of samples was prepared with a 0.02 M precursor concentration at pH 8 and 9 and identified as PMOM-P8 C and PMOM-P9 D, respectively. A schematic illustration of the preparation of the PMOM samples is shown in Scheme 1.

The precipitate obtained in the reaction was identified as $MnCO_3$ by analyzing the Powder X-ray diffraction (P-XRD) data using X'Pert HighScore Plus software, that matches the ICDD data 00-007-0268 (Fig. 1(a)). $MnCO_3$ exhibits a rhombohedral crystal system with unit cell parameters $a = b = 4.8$ Å, $c = 15.7$ Å, $\alpha = \beta = 90°$, and $\gamma = 120°$. The diffraction peaks observed at $2\theta = 24.3°$, 31.5°, 37.6°, 41.5°, 45.3°, 49.8°, 51.6°, 60.3°, 64.1°, 65.5° and 67.9° correspond to the *hkl* values (012), (104), (110), (113), (202), (024), (018), (122), (214), (208) and (300), respectively. The peak indexed to the (104) plane exhibits the highest intensity. Furthermore, to understand the morphology-conserved transformation of the precursor, an SEM image of the $MnCO_3$ precursor (PMOM-P9 B) was obtained, as shown in Fig. 1(b). The precursor exhibited a stacked smooth surface cuboidal structure, with an average side length of 0.4–0.7 μm. Thermogravimetric (TG) analysis of the $MnCO_3$ precursor was conducted and the results are shown in Fig. S1 (ESI†). The significant weight loss observed at 425 °C was attributed to the thermal decomposition of $MnCO_3$ and conversion to Mn_2O_3. The sample weight was stabilized at approximately 550 °C, indicating the need for a calcination temperature above 550 °C for the conversion of $MnCO_3$ to PMOM. Accordingly, the $MnCO_3$ precursors were then calcined at 600 °C for 12 h, resulting in the morphology-conserved transformation of $MnCO_3$ into PMOM.

The P-XRD data of the synthesized PMOM samples are shown in Fig. 2. The observed diffraction peaks were indexed to the ICDD 00-041-1442 pattern, corresponding to cubic Mn_2O_3 or α-Mn_2O_3 ($a = b = c = 9.4$ Å and $\alpha = \beta = \gamma = 90°$). Matching was assessed using X'Pert HighScore Plus software, and no impurity phases were identified in the sample. All the peaks of the samples were in accordance with the cubic crystal system of ICDD 00-041-1442 of bixbyite α-Mn_2O_3, indicating the formation of a single-phase compound. The high-intensity peak observed at 32.9° corresponds to the *hkl* value (222), and the other peaks observed were indexed to the (211), (400), (332), (431), (440), and (622) planes, corresponding to 2θ values of 23.1°, 38.2°, 45.2°, 49.3°, 55.2°, and 65.8°, respectively.

SEM analysis showed a morphology similar to that of the precursor for all PMOM samples. SEM images of samples PMOM-P8 A and PMOM-P9 B are shown in Fig. 3(a) and (b), respectively. Similarly, Fig. 3(c) and (d) represents the SEM images of PMOM-P8 C and PMOM-P9 D, respectively. The formation of PMOM after calcination of the $MnCO_3$ precursor is evident from the SEM images. The particle size distribution histogram was prepared by measuring the size of the particles from the SEM images using ImageJ software. The mean particle sizes of the PMOM samples (Table 2) are shown in the histogram along with their respective SEM images. The mean

Table 1 Different reaction conditions applied for the synthesis of Mn_2O_3

Sample	Concentration of precursor (M)	Concentration of $NaHCO_3$ (M)[a]/(mL)[b]	Reaction temperature (°C)	Reaction pH
PMOM-P8 A	0.1	0.8 M/(25 mL)	90	8
PMOM-P9 B	0.1	1.0 M/(25 mL)	90	9
PMOM-P8 C	0.02	0.8 M/(15 mL)	90	8
PMOM-P9 D	0.02	1.0 M/(20 mL)	90	9

[a] Molarity of the solution. [b] Amount of solution added.

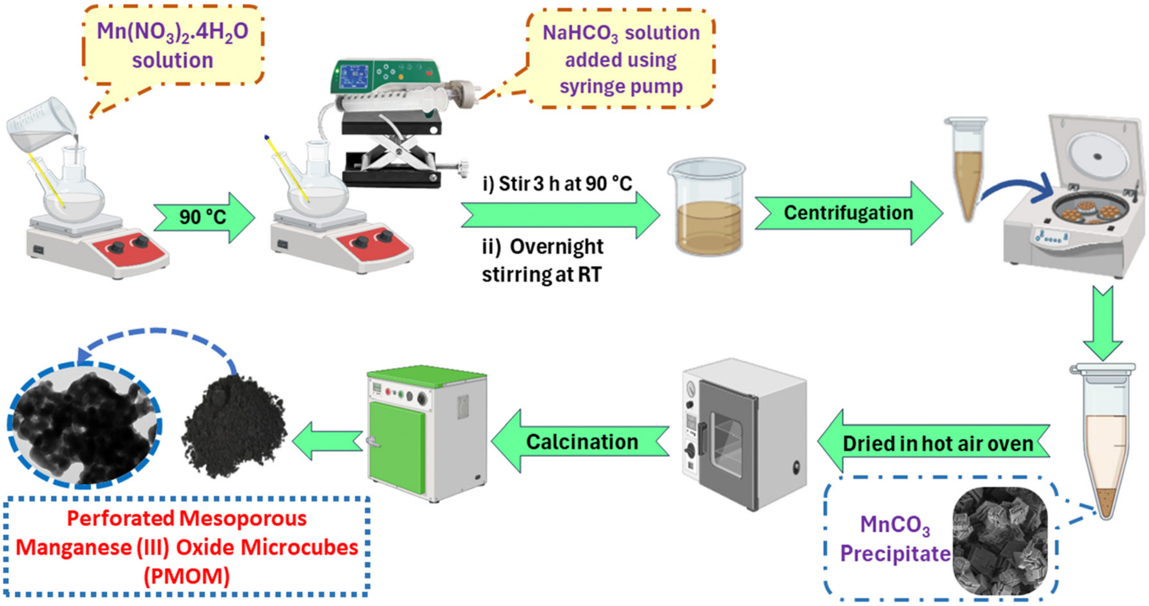

Scheme 1 Schematic representation of the synthesis of PMOM samples.

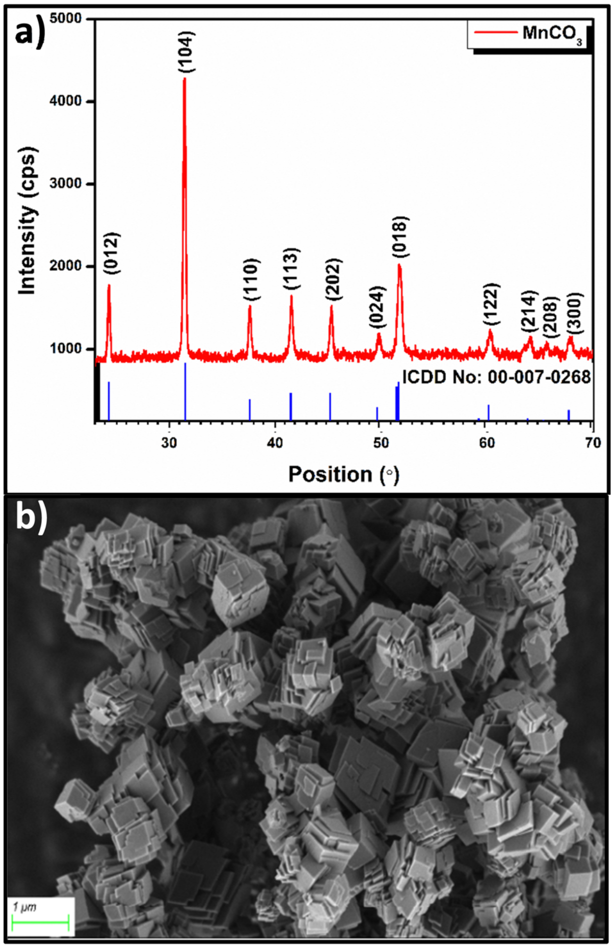

Fig. 1 (a) P-XRD pattern and (b) SEM image of the $MnCO_3$ precursor.

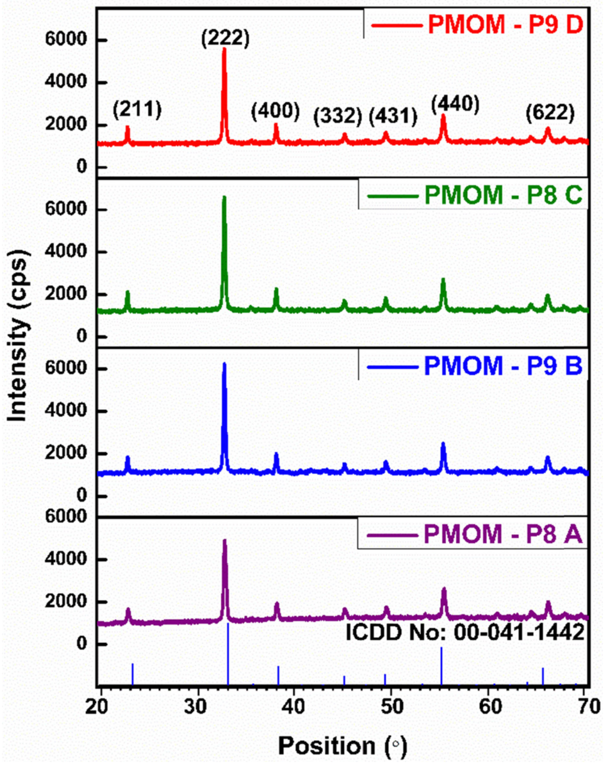

Fig. 2 PXRD pattern of the synthesized PMOM samples.

particle sizes calculated from the SEM images were 0.70 (Fig. 3(e)) and 0.79 μm (Fig. 3(f)) for samples PMOM-P8 A and PMOM-P9 B, respectively, and 0.97 (Fig. 3(g)) and 1.16 μm (Fig. 3(h)) for samples PMOM-P8 C and PMOM-P9 D, respectively. The particle size distribution is narrower for PMOM-P8 A (0.5–1.0 μm) compared to that of other samples. As demonstrated,

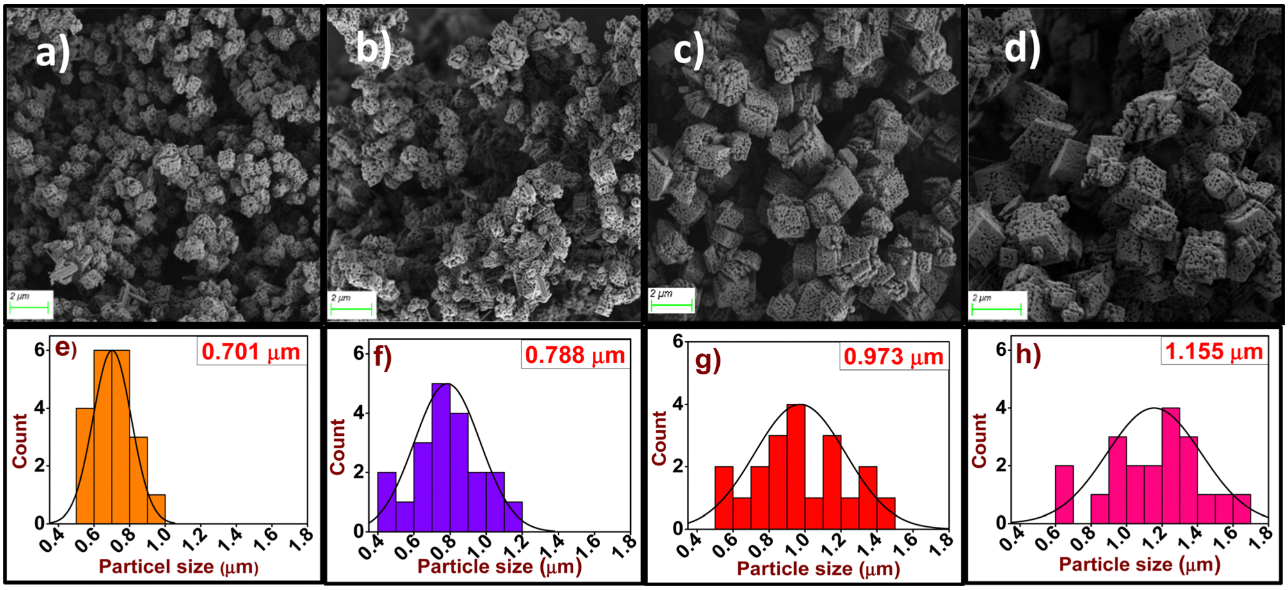

Fig. 3 SEM images of (a) PMOM-P8 A, (b) PMOM-P9 B, (c) PMOM-P8 C and (d) PMOM-P9 D, and particle size distribution histogram of (e) PMOM-P8 A, (f) PMOM-P9 B, (g) PMOM-P8 C and (h) PMOM-P9 D.

Table 2 The mean particle size of the PMOM samples calculated from the SEM and TEM images

Sample	Mean particle size from the SEM image (μm)	Mean particle size from the TEM image (μm)
PMOM-P8 A	0.70	0.75
PMOM-P9 B	0.79	0.74
PMOM-P8 C	0.97	0.95
PMOM-P9 B	1.16	1.21

when the pH of the reaction increased from 8 to 9, the size of the particles increased while maintaining their porous nature. When the precursor concentration was reduced to 0.02 M, the particles adopted more defined cuboidal structures with increased particle size. PMOM-P8 C has a mean particle size of 0.97 μm and the mean particle size increased to 1.16 μm for PMOM-P9 D when the reaction medium became more alkaline.

Fig. 4(a) and (b) show the TEM images of the PMOM sample. The analysis revealed that the Mn_2O_3 samples had a cuboidal shape with a perforated mesoporous structure. From the HRTEM image, it is evident that pores are not only present on the surface of the Mn_2O_3 microcubes, but run through the cube, giving a Swiss cheese-like structure for the particles. The mesopores are visible as low-material-density areas (bright areas) in the TEM images. A series of regular spots were observed in the selected-area electron diffraction (SAED) pattern (Fig. 4(a)). The SAED images were analyzed using Gatan Microscopy Suite software to identify the interplanar spacing and surface phase identification in the PMOM samples. The spots correspond to the (222) plane with a *d*-spacing, $d = 2.7$ Å, corresponding to the high intensity pattern observed at 32.9°. The planes (211) and (440) corresponding to $d = 3.8$ Å and $d = 1.6$ Å were respectively observed at 23.1 and 55.1° in the P-XRD pattern. The HRTEM analysis (Fig. 4(b)) revealed that the exposed surface corresponded to the (211) plane.

The surface area and pore behavior of the synthesized PMOM samples were investigated using a Brunauer–Emmett–Teller (BET) surface analyzer. The specific surface area, total pore volume, and pore size distribution of the catalysts were determined using BET analysis. The BET adsorption–desorption isotherms of the synthesized PMOM samples with the pore distribution curve as an inset are shown in ESI,† Fig. S2–S6. The adsorption–desorption isotherm are classified as type IV based on the IUPAC category with a hysteresis loop at relative pressure (p/p_0) between 0.3 and 1.0, indicating the presence of mesoporous structures. The specific surface areas, average pore diameters and total pore volumes of the samples are listed in Table 3. The pore size distribution, and the pore size were confirmed to be in the mesoporous range (pore sizes between 2 and 50 nm) by the BET studies. The formation of perforated mesoporous microcubes increased the specific surface area of the samples. The PMOM-P9 D sample exhibited a larger pore diameter (27.8 nm) compared to the other samples. The BET surface areas (Table 3) of PMOM-P8 A, PMOM-P9 B, PMOM-P8 C and PMOM-P9 D were measured to be 7.38, 8.05, 6.94 and 6.69 $m^2 g^{-1}$ respectively. It is evident that PMOM-P9 B exhibited the highest surface area. It was also conjectured that the decrease observed in the surface area of samples PMOM-P8 C and PMOM-P9 D, synthesized with a precursor concentration of 0.02 M, can be due to the larger mean particle size. In addition, the samples had total pore volumes in the range of 0.037–0.046 $cm^3 g^{-1}$. The variation in the mean particle size and mean pore diameter with the change in pH, and the change in the precursor concentration, is shown in Fig. 5.

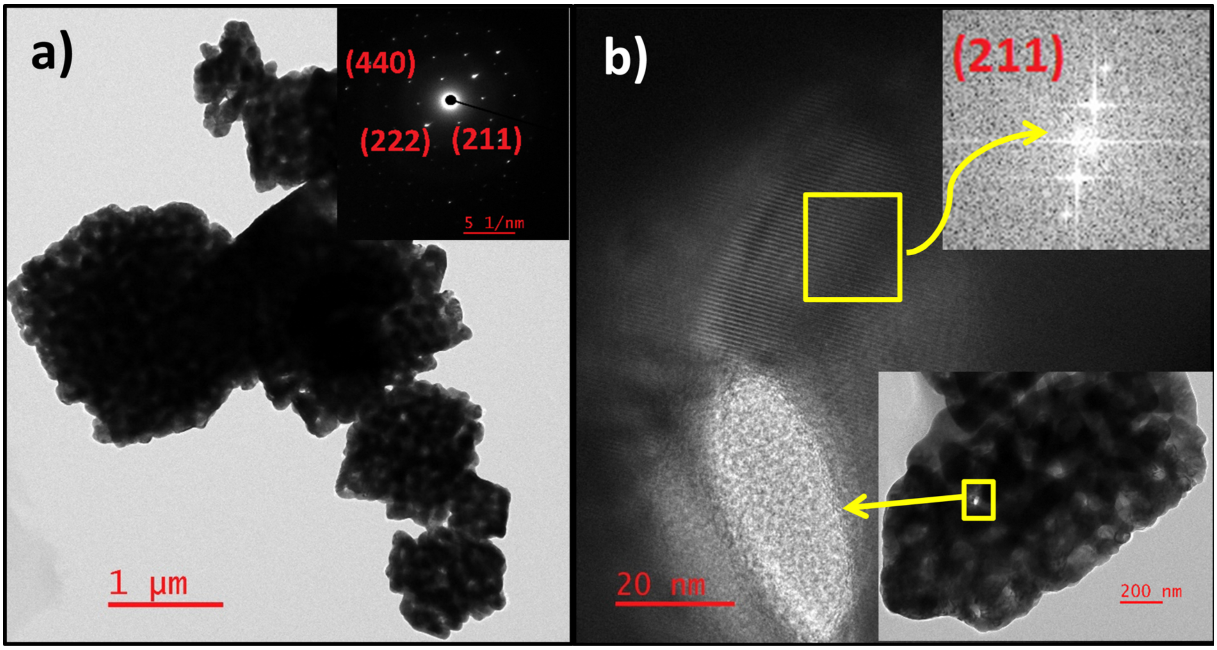

Fig. 4 (a) TEM image with the SAED pattern as the inset. (b) HRTEM image with the corresponding FFT and TEM image showing the perforated mesopores as insets of the PMOM sample.

Table 3 Surface area, pore diameter and pore volume determined by BET analysis of the PMOM samples

Sample	Surface area (m^2 g^{-1})	Mean pore diameter (nm)	Total pore volume (cm^3 g^{-1})
PMOM-P8 A	7.39	23.4	0.043
PMOM-P9 B	8.05	19.3	0.039
PMOM-P8 C	6.94	21.4	0.037
PMOM-P9 D	6.69	27.8	0.046

Concentration and pH play important roles in controlling particle size. Both the mean particle size and the mean pore diameter were larger when the precursor concentration was lower. This could possibly be due to the fact that at a fixed solvent amount, lowering the precursor amount (low concentration) can change the precursor/$NaHCO_3$ interacting ratio, which leads to less nucleation and hence the growth of larger particles. When the concentration of the precursor taken was 0.02 M, the PMOM-P9 D sample with pH = 9 had a larger mean pore diameter (27.8 nm) as well as a higher mean particle size (1.16 µm). However, when the precursor concentration taken was 0.1 M, the mean particle size was higher for PMOM-P9 B at pH 9. The mean particle size decreased from 0.79 µm to 0.70 µm when the pH was reduced to 8 from 9. But the mean pore diameter was larger for PMOM-P8 A with pH = 8, indicating that the mean pore diameter increased from 19.3 nm to 23.4 nm when the pH was reduced to 8 from 9. In Fig. 6, the magnified SEM image of sample PMOM-P9 B shows higher pore density and pore size of the PMOM particles. Using ImageJ software, the sizes of the pores developed on the surface of the microcubes were calculated and marked in the SEM image. The average size was calculated to be 35.34 nm and found to be in good agreement with the BET data obtained.

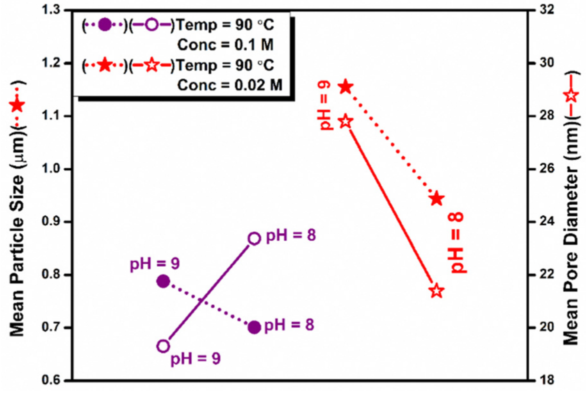

Fig. 5 Variation of mean particle size and mean pore diameter of the PMOM samples with the change in reaction conditions.

FTIR spectrometry was employed to identify the presence of the surface-adsorbed species. In the FTIR spectra (Fig. S7(a) of ESI†), bands in the region of 670–470 cm^{-1} confirmed manganese oxide formation. The peak located at 476 cm^{-1} was attributed to the Mn–O bending vibration, whereas the sharp peaks observed at 563 cm^{-1} and 667 cm^{-1} were due to the stretching vibrations of

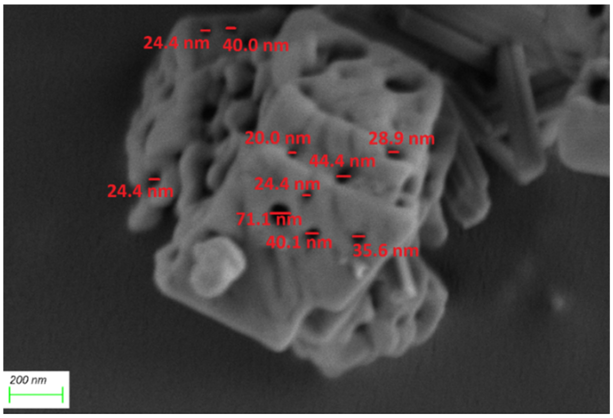

Fig. 6 High magnification SEM image of PMOM-P9 B.

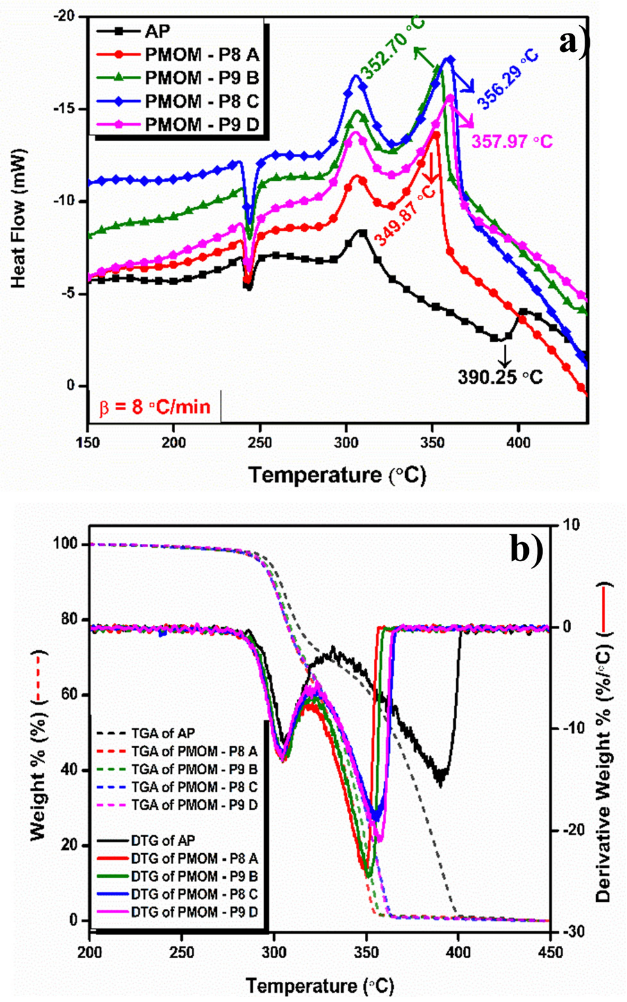

Fig. 7 (a) DTA curves and (b) TG–DTG curves of AP and AP–PMOM samples.

the Mn–O–Mn bond.[21] The stretching vibration of the O–H bond was observed (Fig. S7(b) in ESI†) as a broad band in the region 4000–3500 cm^{-1}, indicating the presence of anchored water molecules adsorbed on the surface. The absorption in the 1800 cm^{-1} region corresponds to the bending vibration of water molecules and confirms the presence of water molecules on the surface. Fig. S9 in the ESI† shows the Raman spectra of the samples. The characteristic peak observed at 630 cm^{-1} was found to be that of the stretching vibration of the Mn–O bond in accordance with the literature values.[21]

Thermocatalytic decomposition of ammonium perchlorate

Ammonium perchlorate (AP) is an extensively used oxidizer in most solid propelled launch vehicles and rockets. The performance of these propellants is significantly influenced by the oxidizer decomposition. The thermal analysis of AP reveals three specific thermal events, and the first is the endothermic peak appearing at 240 °C, indicating the polymorphic transition of AP from orthorhombic phase to cubic phase. This event was followed by two decomposition stages, low-temperature decomposition (LTD) and high-temperature decomposition (HTD).[34] In Fig. S10 (ESI†), the DTA thermogram shows the endothermic phase transition at 244 °C, the LTD peak at 305.14 °C and the HTD peak at 390.25 °C.

Proton transfer is the most accepted mechanism (R1) by which AP is broken down to produce ammonia and perchloric acid as byproducts. LTD corresponds to this dissociative sublimation of AP, and the products NH_3 and $HC1O_4$ are adsorbed on the pores formed on the surface of the non-decomposed AP during partial decomposition. The HTD corresponds to the oxidation of the dissociation products (R2).[35]

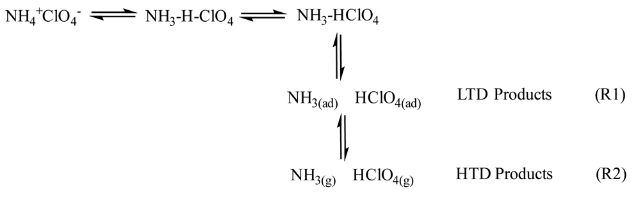

Limited reports exist on the thermocatalytic applications of Mn_2O_3-based catalysts. When mixed with AP, α-Mn_2O_3 with particle sizes of 20–30 nm, 54.3 nm, and 100 nm exhibited HTD peaks at 311 °C,[28] 264 °C[29] and 350.7 °C,[27] respectively. The TG analyses of the AP and AP–PMOM samples were performed, as explained in the experimental section. Thermal decomposition curves of the samples were recorded at a heating rate of 8 °C min^{-1}. The addition of PMOM significantly affected the thermal decomposition of AP. When 2% (by weight) PMOM samples were added to AP, as shown in the DTA (Fig. 7(a)) and TG–DTG curves (Fig. 7(b)), the HTD peak temperature was remarkably reduced to 357.97, 356.29, 352.70 and 349.87 °C, respectively, when PMOM-P9 D, PMOM-P8 C, PMOM-P9 B, and PMOM-P8 A samples were incorporated into AP. The PMOM-P8 A sample, with the lowest mean particle size distribution, significantly reduced the HTD temperature to 349.87 °C, which accounts for a reduction of 40 °C from that of pure AP (Table 4). So, the order of the catalytic activity of PMOM as PMOM-P8 A > PMOM-P9 B > PMOM-P8 C > PMOM-P9 D was confirmed.

In addition to particle size, the porous nature of the PMOM sample influenced the thermal decomposition of AP. The interaction of AP decomposition products with the catalyst is facilitated because of its porous structure; thus, PMOM can

Table 4 Mean particle size, particle size distribution, and LTD and HTD peak temperature of α-Mn_2O_3 samples

Sample	Mean particle size (μm)	Particle size distribution (μm)	LTD peak temperature (°C)	HTD peak temperature (°C)
PMOM-P8 A	0.70	0.5–1.0	303.70	349.87
PMOM-P9 B	0.79	0.4–1.2	304.59	352.70
PMOM-P8 C	0.97	0.5–1.5	304.16	356.29
PMOM-P9 D	1.16	0.6–1.7	304.41	357.97

adsorb the LTD products, leading to further catalysis at the exposed (211) surface and considerably influencing the high-temperature decomposition stage of AP. Earlier studies have reported that Mn_2O_3 reduces the activation energy for the thermal decomposition of AP.[27,29] It can be inferred that during the decomposition reactions, the catalyst acts as a reacting surface for the adsorption of gaseous products and catalyzes surface reactions. The catalytic activity of the mesoporous PMOMs was possibly quantitatively controlled and not phase controlled. Based on the available mechanistic pathways for the catalytic thermal decomposition of AP,[29,36] a plausible mechanism for the catalytic decomposition is proposed and graphically represented in Fig. 8.

It is evident from the IR data that the PMOM samples underwent Mn–HOH surface functionalization. As shown in Fig. S8 (ESI†), the sample adsorbed a considerable number of water molecules from the surroundings, which led to the formation of a large number of Mn–HOH interactions at the surface of the PMOM samples. Manganese can exist in different oxidation states depending on the chemical environment and the possible reduction of Mn^{3+} to Mn^{2+} leads to the oxidation of the surface H_2O molecules to O_2 (R4) by making available electrons and in turn more vacancies on the surface of the PMOM samples. As long as this oxidation–reduction cycle occurs, a considerable number of electrons are available for promoting surface reactions. AP decomposition can be explained based on both proton and electron transfer mechanisms.[37] The electrons are captured by NH_4^+ ions to form NH_3 (R5)[38] and ClO_4^- ions can abstract the generated H^+ ions to form $HClO_4$ (R6).[39] Consequently, more NH_3 and $HClO_4$ were absorbed into the vacancies generated on the catalyst surface. In due course, the active catalyst species promote the electron transfer reaction (R4). This can lead to the rapid surface adsorption of NH_3 and $HClO_4$, and faster decomposition of AP, eventually leading to fast high temperature decomposition of NH_3 and $HClO_4$, forming volatile products such as Cl_2, ClO_2, O_2, NO, and NO_2, resulting in a considerable reduction in the HTD peak temperature.

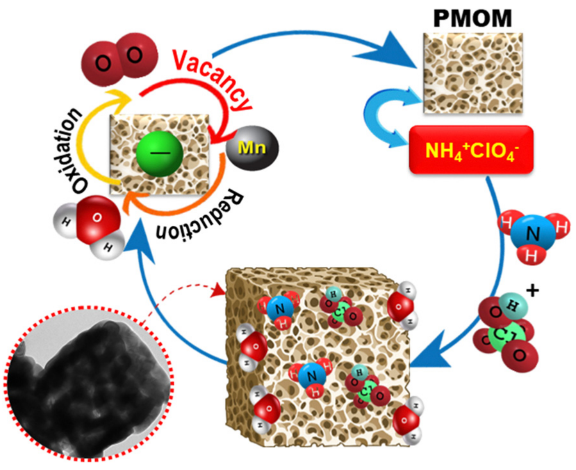

Fig. 8 Possible mechanistic pathway of catalytic thermal decomposition of AP.

$$NH_4^+ClO_4^- \rightleftharpoons ClO_4^-{}_{(ad)} + NH_4^+{}_{(ad)} \quad (R3)$$

$$H_2O_{(ad)} \rightarrow 1/2O_2 + 2H^+_{(ad)} + 2e^- \quad (R4)$$

$$NH_4^+{}_{(ad)} + 1/4O_2 + e^- \rightarrow NH_{3(ad)} + 1/2H_2O\uparrow \quad (R5)$$

$$ClO_4^-{}_{(ad)} + H^+_{(ad)} \rightarrow HClO_4\uparrow \quad (R6)$$

$$4HClO_4 \rightarrow Cl_2 + 2ClO_2 + 5O_2 + 2H_2O \quad (R7)$$

$$2NH_3 + 2ClO_2 \rightarrow N_2O + Cl_2 + 3H_2O \quad (R8)$$

Lowering the temperature of the thermal decomposition of AP is considered a basic requirement for enhancing the burn rate of AP-based propellants. Hence, the incorporation of PMOM having micron sized particles significantly lowered the HTD of AP by promoting the surface reactions. The large specific surface area of PMOM and the active sites generated by the leaving oxygen species on the surface by the reduction of Mn^{3+} to Mn^{2+} ions on the (211) surface of PMOM, are factors that enhance the thermal decomposition of AP.

Conclusions

A morphology-conserved transformation methodology was developed for the synthesis of perforated mesoporous manganese(III) oxide microcubes (PMOM). This template-free method produced PMOM with pore sizes of approximately 20 nm, creating a Swiss-cheese-like structure. HR-TEM analysis showed the perforations as areas of low-density matter, and the lattice fringes confirmed the exposed surface as (211). A significant number of water molecules adsorbed on the PMOM surface indicated Mn–HOH interactions, and the reduction of Mn^{3+} to Mn^{2+} rendered the PMOM surface electron-rich, leading to the oxidation of water molecules on the surface. The porous nature of the PMOM further enhanced the surface activity of the exposed Mn atoms. The low-temperature decomposition (LTD) products of ammonium perchlorate (AP), NH_4^+, and ClO_4^- were possibly adsorbed on the (211) surface, gained electrons, and decomposed into low molecular weight species. The oxidation of ammonia generated water molecules, which followed the same path of adsorption and subsequent oxidation, accelerating the degradation of the LTD products and enhancing the overall decomposition rate of AP. The facile morphology-conserved transformation of the precursor can be applied to develop other TMOs with specific morphologies. It is believed that the catalytic activity of PMOM presented in this study is one example among the many other possible catalytic applications that can be further pursued.

Author contributions

The manuscript was written through contributions of all authors. All authors have given approval to the final version of the manuscript.

Data availability

The data that support the findings of this study are available from the corresponding author upon reasonable request. Data generated and analysed in this study are included in the article and its ESI.†

Conflicts of interest

There are no conflicts to declare.

Acknowledgements

The authors thank the Defense Research and Development Organization [DRDO/ARMREB/HEM/2021/241], Science and Engineering Research Board [SERB/SRG/2021/001182] and FRG NIT Calicut for their financial support. The authors thank the University of Hyderabad for extending the TEM facility and the Centre for Materials Characterization (CMC)-NIT Calicut for the PXRD facility.

References

1 R. Zeng, Q. Gao, L. Xiao, W. Wang, Y. Gu, H. Huang, Y. Tan, D. Tang and S. Guo, *J. Am. Chem. Soc.*, 2024, **146**, 10023–10031.
2 Z.-R. Tian, W. Tong, J.-Y. Wang, N.-G. Duan, V. V. Krishnan and S. L. Suib, *Science*, 1979, **1997**(276), 926–930.
3 Y. Xue, S. Sun, Q. Wang, Z. Dong and Z. Liu, *J. Mater. Chem. A*, 2018, **6**, 10595–10626.
4 S. Park, Y. H. Lee, S. Choi, H. Seo, M. Y. Lee, M. Balamurugan and K. T. Nam, *Energy Environ. Sci.*, 2020, **13**, 2310–2340.
5 Z.-R. Tian, W. Tong, J.-Y. Wang, N.-G. Duan, V. V. Krishnan and S. L. Suib, *Science*, 1979, **1997**(276), 926–930.
6 G. Zhang, X. Li, Y. Liu, G. Du and H. Pang, *Inorg. Chem. Front.*, 2024, DOI: 10.1039/D4QI01732C.
7 C. Shamjitha and A. A. Vargeese, *ACS Appl. Nano Mater.*, 2024, **7**, 8557–8566.
8 G. He and Y. Liao, *J. Mater. Chem. A*, 2023, **11**, 6688–6746.
9 S. Sanati, A. Morsali and H. García, *Energy Environ. Sci.*, 2022, **15**, 3119–3151.
10 Z. Yang, X. Yu, J. Zhao, R. Wang, C. Zhang and H. Cao, *New J. Chem.*, 2024, DOI: 10.1039/D4NJ03002H.
11 C.-T. Hung, L. Duan, T. Zhao, L. Liu, Y. Xia, Y. Liu, P. Qiu, R. Wang, Z. Zhao, W. Li and D. Zhao, *J. Am. Chem. Soc.*, 2022, **144**, 6091–6099.
12 Z. Lv, L. Zhu, Z. Yin, M. Li and D. Tang, *Anal. Chim. Acta*, 2021, **1171**, 338680.
13 Y. Lin, Q. Zhou and D. Tang, *Anal. Chem.*, 2017, **89**, 11803–11810.
14 I. M. Mosa, S. Biswas, A. M. El-Sawy, V. Botu, C. Guild, W. Song, R. Ramprasad, J. F. Rusling and S. L. Suib, *J. Mater. Chem. A*, 2016, **4**, 620–631.
15 S. Zhu, S.-H. Ho, C. Jin, X. Duan and S. Wang, *Environ. Sci.: Nano*, 2020, **7**, 368–396.
16 P. Li, C. Nan, Z. Wei, J. Lu, Q. Peng and Y. Li, *Chem. Mater.*, 2010, **22**, 4232–4236.
17 A. Vázquez-Olmos, R. Redón, G. Rodríguez-Gattorno, M. Esther Mata-Zamora, F. Morales-Leal, A. L. Fernández-Osorio and J. M. Saniger, *J. Colloid Interface Sci.*, 2005, **291**, 175–180.
18 T. He, S. Rong, D. Ding, Y. Zhou, N. Zhang and W. He, *ACS Catal.*, 2023, **13**, 8049–8062.
19 F. Jiao, A. Harrison, A. H. Hill and P. G. Bruce, *Adv. Mater.*, 2007, **19**, 4063–4066.
20 Q. Zhao and W.-H. Shih, *Microporous Mesoporous Mater.*, 2002, **53**, 81–86.
21 P. R. Jothi, M. Pramanik, C. Li, S. Kannan, V. Malgras, R. R. Salunkhe and Y. Yamauchi, *Chem. – Asian J.*, 2016, **11**, 667–673.
22 Y. Qiu, G.-L. Xu, K. Yan, H. Sun, J. Xiao, S. Yang, S.-G. Sun, L. Jin and H. Deng, *J. Mater. Chem.*, 2011, **21**, 6346.
23 A. A. Vargeese, S. S. Joshi and V. N. Krishnamurthy, *Cryst. Growth Des.*, 2008, **8**(3), 1060–1066, DOI: 10.1021/cg070464.
24 K. Chatragadda and A. A. Vargeese, *Combust. Flame*, 2017, **182**, 28–35.
25 L. Li, X. Sun, X. Qiu, J. Xu and G. Li, *Inorg. Chem.*, 2008, **47**, 8839–8846.
26 M. A. Fertassi, K. T. Alali, Q. Liu, R. Li, P. Liu, J. Liu, L. Liu and J. Wang, *RSC Adv.*, 2016, **6**, 74155–74161.
27 J. Liang, J. Yang, W. Cao, X. Guo, X. Guo and W. Ding, *J. Nanosci. Nanotechnol.*, 2015, **15**, 7229–7234.
28 D. Jing, D. Chen, G. Fan, Q. Zhang, J. Xu, S. Gou, H. Li and F. Nie, *Cryst. Growth Des.*, 2016, **16**, 6849–6857.
29 I. P. S. Kapoor, P. Srivastava and G. Singh, *Propellants, Explos., Pyrotech.*, 2009, **34**, 351–356.
30 C. Peng, D. Yu, L. Wang, X. Yu and Z. Zhao, *J. Mater. Chem. A*, 2021, **9**, 12947–12980.
31 P. Kar, S. Sardar, S. Ghosh, M. R. Parida, B. Liu, O. F. Mohammed, P. Lemmens and S. K. Pal, *J. Mater. Chem. C*, 2015, **3**, 8200–8211.
32 L. Zhang, D. Ge, H. Geng, J. Zheng, X. Cao and H. Gu, *New J. Chem.*, 2017, **41**, 7102–7107.
33 M. R. Shaik, R. Syed, S. F. Adil, M. Kuniyil, M. Khan, M. S. Alqahtani, J. P. Shaik, M. R. H. Siddiqui, A. Al-

Warthan, M. A. F. Sharaf, A. Abdelgawad and E. M. Awwad, *Saudi J. Biol. Sci.*, 2021, **28**, 1196–1202.

34 S. Vyazovkin and C. A. Wight, *Chem. Mater.*, 1999, **11**, 3386–3393.

35 V. V. Boldyrev, *Thermochim. Acta*, 2006, **443**, 1–36.

36 P. Gong, J. Xie, D. Fang, F. He, F. Li and K. Qi, *Mater. Res. Express*, 2017, **4**, 115036.

37 A. G. Keenan and R. F. Siegmund, *Q. Rev., Chem. Soc.*, 1969, **23**, 430.

38 M. J. Trenerry, C. M. Wallen, T. R. Brown, S. V. Park and J. F. Berry, *Nat. Chem.*, 2021, **13**, 1221–1227.

39 R. Dalpozzo, G. Bartoli, L. Sambri and P. Melchiorre, *Chem. Rev.*, 2010, **110**, 3501–3551.